



Discovery of the First Quadruple Gravitationally Lensed Quasar Candidate with Pan-STARRS

C. T. Berghea¹, George J. Nelson¹, C. E. Rusu², C. R. Keeton³, and R. P. Dudik¹

¹ U.S. Naval Observatory (USNO), 3450 Massachusetts Avenue NW, Washington, DC 20392, USA; ciprian.t.berghea@navy.mil

² Department of Physics, University of California, Davis, 1 Shields Avenue, CA 95616, USA

³ Department of Physics & Astronomy, Rutgers, the State University of New Jersey, 136 Frelinghuysen Road, Piscataway, NJ 08854, USA

Received 2017 May 18; revised 2017 June 16; accepted 2017 June 18; published 2017 July 26

Abstract

We report the serendipitous discovery of the first gravitationally lensed quasar candidate from Pan-STARRS. The *grizy* images reveal four point-like images with magnitudes between 14.9 and 18.1 mag. The colors of the point sources are similar, and they are more consistent with quasars than with stars or galaxies. The lensing galaxy is detected in the *izy* bands, with an inferred photometric redshift of ~ 0.6 , lower than that of the point sources. We successfully model the system with a singular isothermal ellipsoid with shear, using the relative positions of the five objects as constraints. While the brightness ranking of the point sources is consistent with that of the model, we find discrepancies between the model-predicted and observed fluxes, likely due to microlensing by stars and millilensing due to the dark matter substructure. In order to fully confirm the gravitational lens nature of this system and add it to the small but growing number of the powerful probes of cosmology and astrophysics represented by quadruply lensed quasars, we require further spectroscopy and high-resolution imaging.

Key words: cosmology: observations – gravitational lensing: strong – quasars: general

1. Introduction

Since the serendipitous discovery of the first gravitationally lensed quasar (Walsh et al. 1979), these systems have become powerful probes of astrophysics and cosmology, as illustrated by the wealth of science they have provided over the years. For example, Peng et al. (2006) and Ding et al. (2017) have studied the coevolution of supermassive black holes and the quasar hosts harboring them up to high redshift (Claeskens & Surdej 2002; Treu 2010). Oguri et al. (2012), Bonvin et al. (2017), and others have constrained the cosmological constant and the Hubble constant from samples of lensed quasars (see the recent review by Treu & Marshall 2016). Flux ratio anomalies have revealed luminous satellites or set constraints on the dark matter substructure in the lensing galaxies (e.g., Chiba et al. 2005; McKean et al. 2007; Fadely & Keeton 2012). Ensembles of lenses have revealed the structure of massive galaxies (e.g., Kochanek et al. 2000; Oguri et al. 2014). Other insights into quasar accretion disks (e.g., Dai et al. 2010), broad-line regions (e.g., Sluse et al. 2012), and black hole spin (Reis et al. 2014) have been gained.

These applications all require increasingly large samples of lensed quasars, and in particular, quadruply lensed quasars (quads), due to the increased number of modeling constraints they provide. To date, there are only about three dozen known quads over the whole sky.⁴ Due to the rare nature of lensed quasars, large-scale surveys of sufficient depth and resolution are required to significantly increase the present sample (Oguri & Marshall 2010). As such surveys have become available, pioneering searches for lensed quasars, such as the Cosmic Lens All Sky Survey (CLASS; Myers et al. 2003) have been succeeded by the SDSS Quasar Lens Search (SQLS; Oguri et al. 2006), and more recently by the STRong lensing Insight in the Dark Energy Survey (STRIDES; Agnello et al. 2015)

and the extension to SQLS using the Baryon Oscillation Spectroscopic Survey (BQLS; More et al. 2016), among others.

In this paper, we report the serendipitous discovery of a quadruply lensed quasar candidate from the Panoramic Survey Telescope and Rapid Response System (Pan-STARRS1, hereafter PS1) released images. The lensed quasar was discovered as part of a variability study of active galactic nuclei selected based on mid-infrared characteristics (Secrest et al. 2015) and data from the USNO Robotic Astrometric Telescope (URAT; Zacharias et al. 2015). To our knowledge, if proven with spectroscopic observations, this would be the first published gravitational lens discovered in the PS1 data. We note that this system is very similar to the well-studied quad lens RX J1131-1231 (Sluse et al. 2003) in terms of image separation and overall configuration. We model the system to provide evidence in support of its lensing nature, and we conclude with the necessity of obtaining spectroscopic confirmation. Due to its position, this is not possible from the ground until the end of the year.

PS1 is a wide-field imaging system, with a 1.8 m telescope and 7.7 deg² field of view (FOV), located on the summit of Haleakala in the Hawaiian island of Maui. The first PS1 data were released in 2016 December, including both images and catalogs (see Chambers et al. 2016). The 1.4 Gpixel camera consists of 60 CCDs with a pixel size of 0.256 arcsec (Onaka et al. 2008; Tonry & Onaka 2009). It uses five filters (g_{P1} , r_{P1} , i_{P1} , z_{P1} , y_{P1} , hereafter *grizy*), similar to the ones used by the Sloan Digital Sky Survey (SDSS; York et al. 2000). The largest survey PS1 performs is the 3 π survey, covering the entire sky north of -30 deg decl. Given the large sky coverage, resolution, and depth, PS1 is expected to contain nearly 2000 gravitationally lensed quasars, of which about 300 will be quadruply lensed quasars (Oguri & Marshall 2010).

The structure of the paper is as follows. In Section 2, we measure the relative astrometry, photometry, and morphology of this system. In Section 3, we infer photometric redshifts, and in Section 4, we conduct a photometric variability study to

⁴ <http://masterlens.astro.utah.edu/>

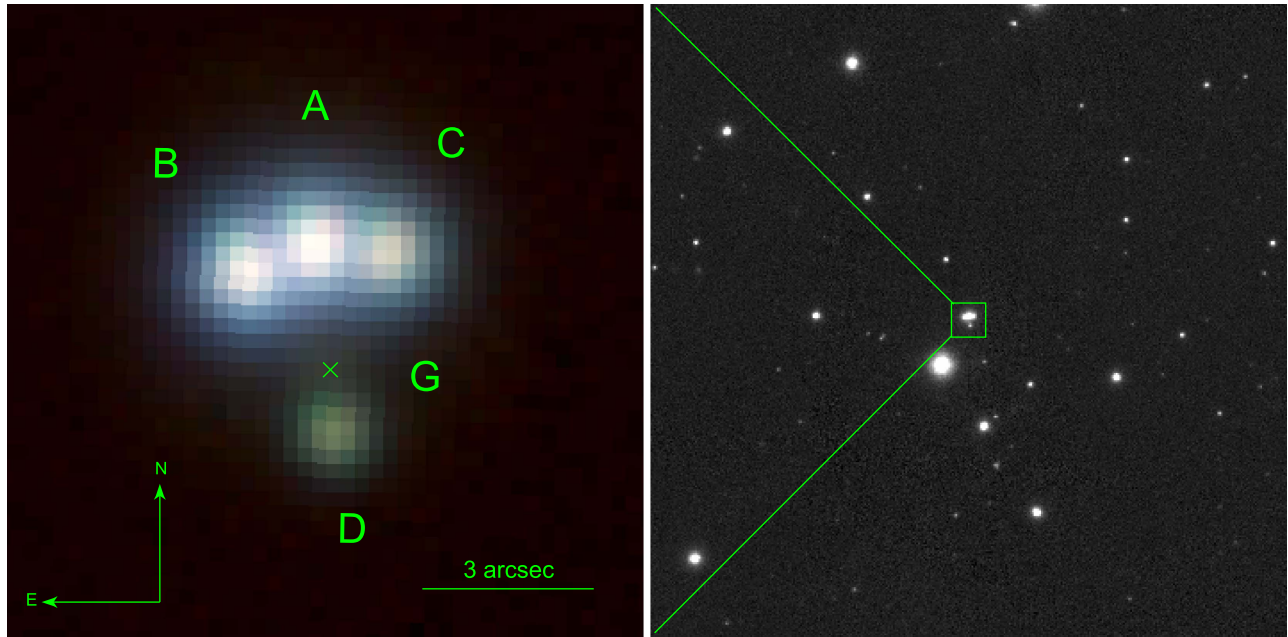


Figure 1. PS1 images of the lens candidate showing the four quasar images A–D with the lensing galaxy position G marked with an \times . Left: close-up color image using the g (blue), i (green), and y (red) filters. The *Gaia* position for component D (26.792307, 46.511273) is used as the absolute astrometric reference position for this system. Right: y -band image of a $2'$ region around the system. The bright star southeast of the lens is saturated in the other bands.

support the photometric redshifts. In Section 5, we fit a lensing mass model to the system. We present our conclusions and future works in Section 6. We assume a cosmological model with $\Omega_M = 0.274$, $\Omega_L = 0.726$, and $h = 0.71$. All magnitudes are in the AB system except for the *WISE* ones, which are in the Vega system.

2. Astrometry, Photometry, and Morphology

We used the stacked images from PS1 in all five filters in order to perform a morphological modeling. We present a close-up color image of the system in Figure 1, which clearly shows four objects within $\lesssim 3''.8$ of each other. The three brightest of these (A, B and C) are arranged in an arc-like configuration. The PS1 catalog identifies only the sources A and D, with B and C being blended with A.

The simple modeling with a point-spread function (PSF) constructed from stars in the PS1 FOV left large residuals at the locations of the four objects, which were significant enough to affect the derived parameters. We suspect that this is due to the spatial variation in the PSF across the PS1 FOV, and have therefore adopted a technique of fitting the system with an analytical PSF, which, it is assumed, will not change on the small scale represented by the system. We did this using Hostlens (Rusu et al. 2016), a variant of glafic (Oguri 2010) that uses χ^2 minimization in order to fit point sources as well as Sérsic (1963) profiles convolved with an analytical PSF. The analytical PSF comprises two concentric Moffat (1969) profiles, each one with its own FWHM, ellipticity, orientation, and shape parameter. The two profiles are also characterized by the relative flux of one to the other. We successfully modeled the four objects as point sources convolved with the PSF, therefore showing that they are point like. Our strategy was to run Hostlens starting from 100 different positions in the parameter space, select the best of the resulting models, and further run 10 Markov Chain Monte Carlo (MCMC) chains using the Metropolis–Hastings algorithm around it. The chains

consist of one million steps, with an acceptance rate of ~ 0.3 , and we removed the first one-fifth of these (the “burn-in” steps). We also checked that the chains have converged, using the method of Gelman et al. (1995). The MCMC-derived uncertainties between the various analytical parameters are shown in Figure 2, and generated using corner.py (Foreman-Mackey 2016). In order to quantify the additional uncertainties inherent in our method due to the non-analytical nature of the “true” PSF, we ran 100 simulations where we added the noise of similar properties to the real images on top of the best-fit model. Here, we created the best-fit model by using a PSF constructed from nearby stars, and we ran Hostlens on each of the 100 simulations, using an analytical PSF. As a final estimate of our uncertainties, we used the maximum between the MCMC-derived uncertainties and those from the simulations. We were able to obtain much improved residuals in all bands, and we show these in Figure 3.

Figure 3 shows conspicuous residuals in the i , z , and y bands (middle row). These are consistent with the discovery of a lensing galaxy, in support of the lensing nature of this system. Due to the relatively low signal-to-noise ratio and the proximity of the point sources, we were unable to fit the morphology of this galaxy with free parameters. The red colors, suggested by the non-detection in the bluer bands, suggest that it is a red, early-type galaxy. As a result, we modeled it with a Sérsic index of 4, typical of early-type galaxies. We checked that this produces a better fit than a Sérsic index of 1. For the Sérsic profile, we used an axis ratio of 1 and we fixed the effective radius at $0''.5$. As the galaxy is most conspicuous in the i and y bands, we consider the most reliable estimate of the relative positions of all objects to be derived from the weighted average of the positions measured in these two bands, where we weight by the inverse of the measured uncertainties. The resulting astrometry and photometry in each band are shown in Table 1. We have corrected the magnitudes for galactic extinction using the maps of Schlafly & Finkbeiner (2011).

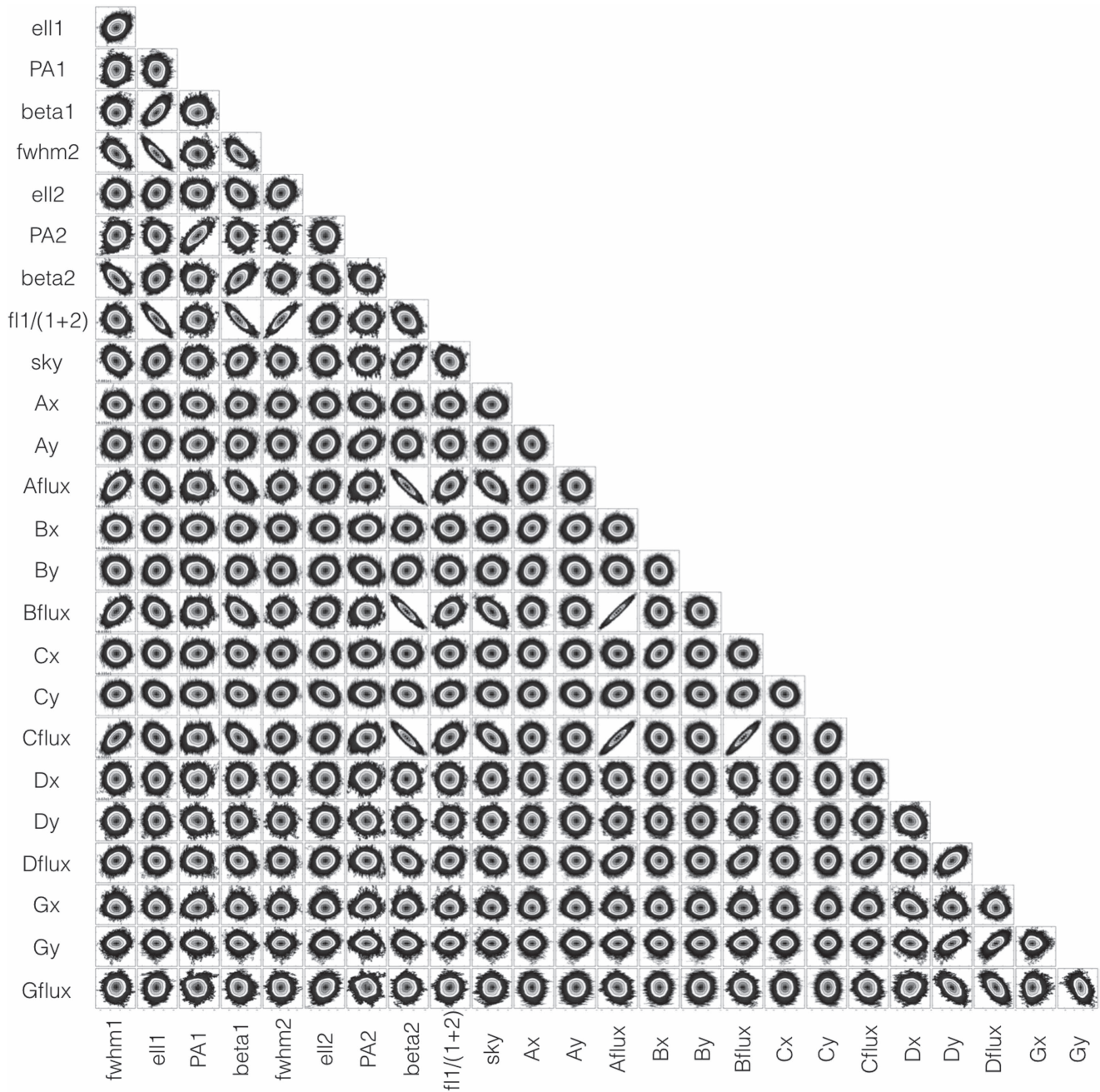


Figure 2. Covariances between the parameters used to model the observed system in the *i* band with Hostlens. The three contour lines mark the 1σ , 2σ , and 3σ limits. The parameters are, in order, the FWHM in arcseconds, ellipticity, orientation, the shape of the first Moffat profile (1, 2, 3, 4), the same for the second Moffat profile (5, 6, 7, 8), the relative flux as $\text{flux1}/(\text{flux1} + \text{flux2})$ (9), sky level in counts (10), positions in pixels on the x and y axes of point source A (11, 12) and its flux in counts (13), and the same for objects B, C, and D (14–25).

In addition to the PS1 data, we also looked for archival data of this system. The system is detected in both the *Gaia* (Gaia Collaboration et al. 2016) DR1 and PS1 catalogs; however, objects A, B, and C are blended into a single object by the automatic pipeline. PS1 psf magnitudes for A are in general smaller than what we obtained, probably due to blending, but for D they are very similar to our uncorrected magnitudes: 18.599 ± 0.013 , 18.153 ± 0.002 , 18.079 ± 0.007 , 17.843 ± 0.0093 , and 17.534 ± 0.023 in the *grizy* bands, respectively. We use the *Gaia* position for component D as the absolute astrometric reference position for this system: 26.792307 , 46.511273 . The errors for these coordinates given in the *Gaia* catalog are 15.6 and 8.9 mas, respectively.

The system is also bright in the infrared, with the unresolved magnitudes being 11.524 ± 0.022 , 10.434 ± 0.020 , 6.769 ± 0.015 , and 4.518 ± 0.023 in the *WISE* bands—W1, W2, W3, and W4, respectively.

Finally, the system is very likely also a radio source. The NRAO VLA Sky Survey (NVSS) images show a source, 2MASX J01471020+4630433, with flux 12.6 mJy at 1.4 GHz. The listed position for this source is only $3''$ away from the center of the system in the optical bands, which is comparable with NVSS astrometric errors (Condon et al. 1998). We are currently in the process of further observing the system in the radio with the Very Large Array (VLA). Radio data are useful for the study of lensed quasars, as it provides

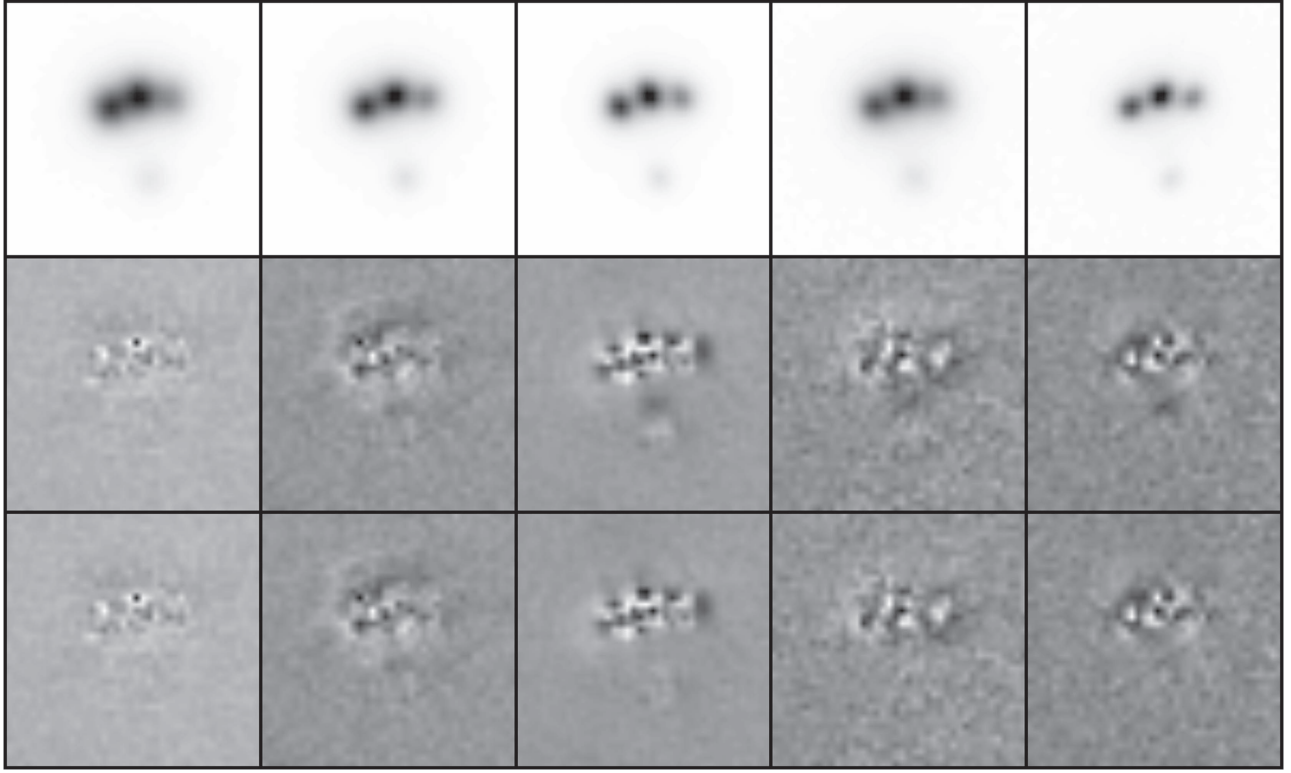


Figure 3. Original images ($10'' \times 10''$, first row) and residuals after subtracting the best-fit model with Hostlens. From left to right: g , r , i , z , and y bands. In the second row, the lensing galaxy is not included in the modeling, whereas in the third row it is. The images are in linear scale and cover the full dynamic range. The remaining structure in the residuals amounts to less than 6% of the peak fluxes and can be attributed to the large Poisson noise at the center of the point-like images, as well as to the faint arcs expected from the lensed quasar host galaxy, which are not accounted for in the modeling.

Table 1
Relative Astrometry and Photometry

Property	A (S1)	B (M2)	C (M1)	D (S2)	G
Measurements					
g	15.60 ± 0.01	15.72 ± 0.01	16.45 ± 0.02	18.09 ± 0.01	...
r	15.40 ± 0.01	15.55 ± 0.01	16.21 ± 0.01	17.74 ± 0.01	...
i	15.36 ± 0.01	15.57 ± 0.02	16.15 ± 0.02	17.74 ± 0.02	19.50 ± 0.20
z	15.23 ± 0.03	15.50 ± 0.05	16.02 ± 0.01	17.68 ± 0.03	18.95 ± 0.13
y	14.92 ± 0.01	15.23 ± 0.02	15.76 ± 0.02	17.36 ± 0.02	19.20 ± 0.24
$\Delta\alpha\cos(\delta)$	0.000 ± 0.004	-1.185 ± 0.004	1.271 ± 0.005	0.410 ± 0.004	0.240 ± 0.050
$\Delta\delta$	0.000 ± 0.004	-0.441 ± 0.004	-0.074 ± 0.004	-3.310 ± 0.004	-2.310 ± 0.025
Model Prediction					
Δm	0.0	$0.580^{+0.17}_{-0.020}$	$0.626^{+0.005}_{-0.009}$	3.55 ± 0.06	

Note. The first four columns are the four quasar images and the fifth column is the lens. We also label the images according to the arrival time. The first five rows are the magnitude measurements derived using Hostlens, corrected for extinction. The next two rows are the relative positions of each object relative to A. We assume a pixel scale of $0''.256$. $\Delta\alpha$ is positive toward the west, and $\Delta\delta$ toward the north. The last row shows the model prediction for the relative magnitudes relative to image A, from the best-fit mass model.

high-resolution imaging of the source, as well as fluxes not affected by microlensing and extinction.

3. Photometric Redshifts

We fit the photometry measured in Section 2 for the point-like sources and the faint red galaxy using spectral energy distribution (SED) templates. The colors of the point-like images are very similar (Table 1), consistent with being multiple images of the same source. Due to their point-like

morphology, we suspect these to be quasars and have therefore fit them with quasar templates in order to check the quality of the fit and to infer photometric redshifts. Photometric redshifts of quasars are notoriously difficult to constrain, due to the relatively featureless continua (Richards et al. 2009) and the variable equivalent widths of the broad emission lines. We measured redshifts using several methods.

1. The method of Wu & Jia (2010) uses derived quasar colors as a function of redshifts. This is based on SDSS

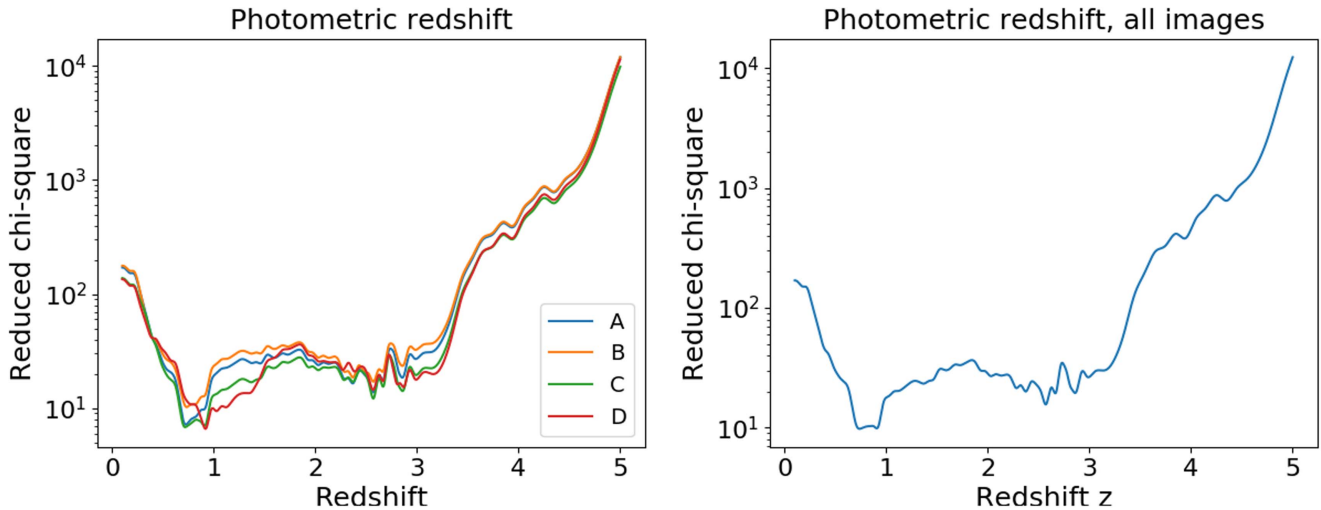


Figure 4. Photometric redshift estimates using the method in Wu & Jia (2010). Left: individually for each image; right: for all images simultaneously.

colors. PS1 bands are similar but not identical to the SDSS bands, and we used the corrections of Finkbeiner et al. (2016) to obtain magnitudes in the SDSS system. Following Wu & Jia (2010), we minimized χ^2 to obtain redshifts for each of the point sources. We only used three of the colors as the Y band from UKIRT is very different from the PS1 y band. We plot χ^2_ν in Figure 4 for each quasar image, and also by fitting all sources together. We notice that the curves are quite consistent with each other, as expected from the similar colors of the sources. In the latter case, we obtain the best fit at $z = 0.820^{+0.018}_{-0.014}$. We notice a second minimum at $z \sim 2.6$. The χ^2_ν for the minima is large, which could be due to the large spread seen in the colors of Wu & Jia (2010). We note that no numerical uncertainties are listed in that paper for the derived colors. We have also explored incorporating a prior based on the quasar luminosity function, given the unmagnified observed magnitudes of the source (see Section 5). While the prior prefers low-redshift values, its effect on Figure 4 is negligible.

2. A second method uses the photometric redshift code LePhare (Arnouts et al. 1999; Ilbert et al. 2006) to fit a quasar template to the observed colors. We obtain the best fit at a redshift of ~ 2.6 – 2.8 for all four point sources. These results agree with the second peak of the method above. The χ^2 is between 13 and 125 for four degrees of freedom (five filters). We find poorer fits (larger χ^2) when using stellar or galactic SED templates, providing further support that the sources are quasars. In particular, the best-fit galaxy templates correspond to starburst galaxies at low redshift $\lesssim 0.1$. At such low redshifts, the sources would likely be resolved, not point like.
3. A combination of SDSS and *WISE* photometry provides good discriminators between high- and low-redshift quasars. DiPompeo et al. (2015) used the ratio between the *WISE* W1 and W2 bands to the i -band flux, and found that high values are expected for quasars below a redshift of 1. We added the fluxes for A, B, C, and D in the i band (to account for the fact that the system is not resolved in *WISE*; G is of negligible flux), and we obtained a total magnitude of 14.4. We obtain ratios $W1/i = 14.4$ and $W2/i = 39.0$, which both indicate a redshift > 2 and are not compatible with the low value of ~ 0.8 , which would

require ratios of $W1/i = 50$ and $W2/i = 120$. We also used the diagnostics from Wu et al. (2012). As seen in Figure 13 of that paper, the colors $z - W1$ and $W2 - W3$ discriminate well between low and high redshift. We obtain $z - W1 = 2.8$ and $W2 - W3 = 3.7$, which both suggest a redshift larger than 2. Our low value of 0.8 would require $z - W1 = 4.0$ and $W2 - W3 = 3.0$.

The lens galaxy G is very faint but we managed to fit a galaxy SED with an early-type template, resulting in a best-fit $z = 0.57^{+0.20}_{-0.13}$. For this, we used the magnitudes measured in the izy bands and assumed detection limits of 21 mag in the gr bands, ~ 2 mag fainter than the rest. We independently checked that the observed magnitudes are reasonable for a redshift of $z = 0.57$: for this redshift, the observed magnitudes imply an absolute magnitude of about $-23.0 \sim -23.5$ in the R band. From the Faber–Jackson relation (Faber & Jackson 1976), using the velocity dispersion we estimate from the lens modeling in Section 5, we obtain $R \sim -23.6$, which is therefore not inconsistent.

4. URAT Variability

Here we undertake a quasar variability study as an independent check of the redshift estimate we derived in the previous section. URAT1 was a U. S. Naval Observatory project designed to provide accurate astrometry in the northern hemisphere down to about 18 mag. A single filter centered at ~ 720 nm was used, which is almost as red as the PS1 i filter. Observations at the Flagstaff Station over more than three years provided more than 50 epochs for a large number of objects.

To characterize the variability of this system, we used a typical method used for quasars, the structure function V , as presented in Vanden Berk et al. (2004). It uses the magnitude differences between different epochs of observation to estimate the variability at different time intervals (time lag). It is defined as

$$V = \left(\frac{\pi}{2} \langle |\Delta m|^2 \rangle - \langle \sigma^2 \rangle \right)^{\frac{1}{2}}, \quad (1)$$

where Δm is the measured magnitude difference for each pair of epochs in the light curve, σ is the statistical measurement uncertainty of Δm , and the brackets denote average quantities.

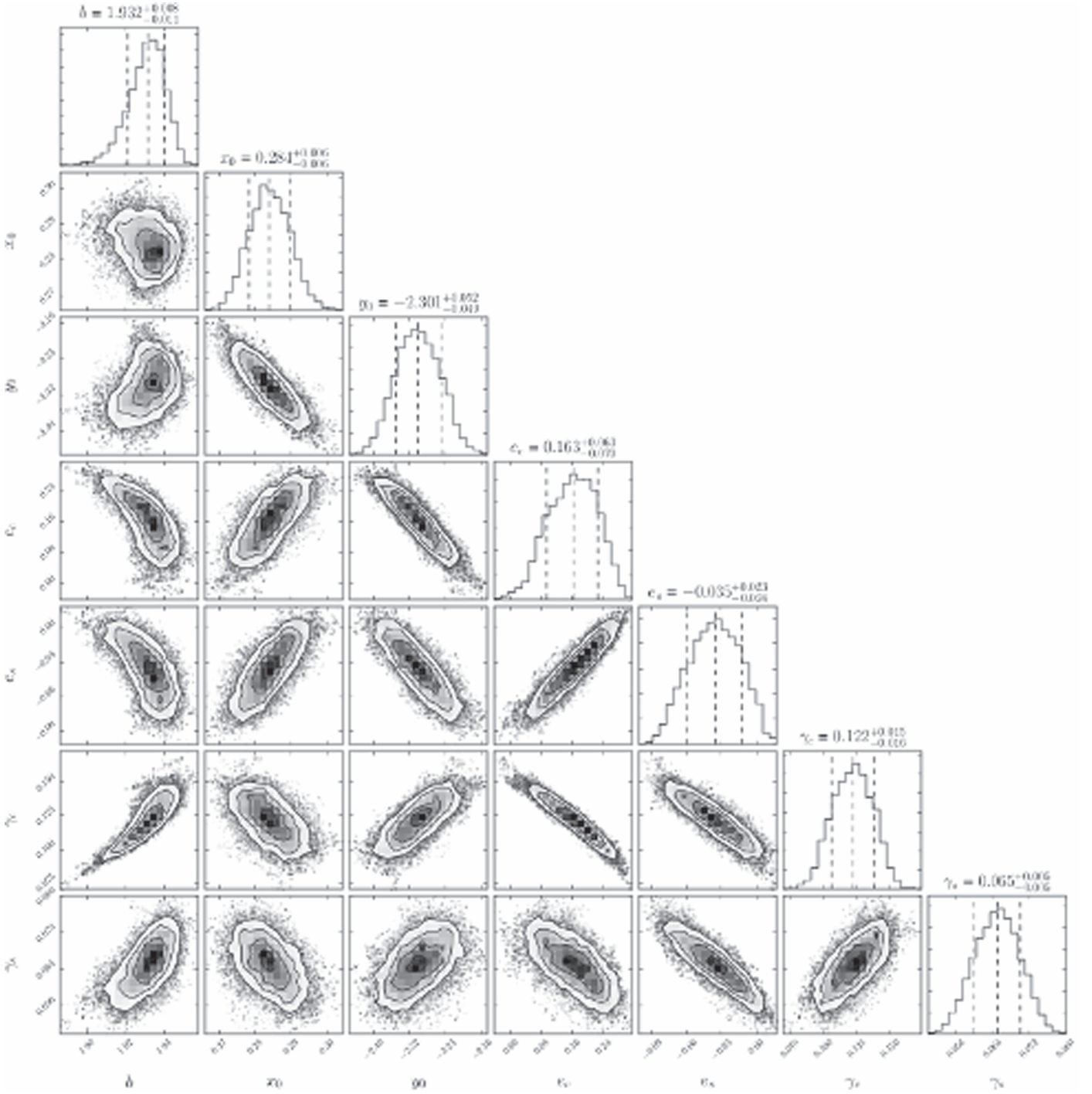


Figure 5. Covariances between the parameters used to model the observed system with lensmodel. The three contour lines mark the 1σ , 2σ , and 3σ limits. The vertical lines in the histograms mark the 16th, 50th, and 84th percentiles. The parameters are, in order, the Einstein radius, lensing galaxy x and y positions, two parameters for ellipticity, and two for shear.

Vanden Berk et al. (2004) used the structure function to characterize the variability of a large sample of SDSS quasars. We note that their study is statistical in nature and therefore only provides general properties which we use to try to discriminate between the two photometric redshifts we obtained in the previous section.

In order to improve the results, we performed relative photometry of URAT epoch data using nearby stars in the 12–14 mag range. We removed stars that show variability and also removed some poor quality observations. We used more

than 50 stars and 36 epochs spanning over two years. We estimate errors using the nearby stars with similar magnitudes. We obtained $V = 0.074$ and an average time lag of 297 days. According to Figure 16 of Vanden Berk et al. (2004), this V value matches quasars at about $z = 2$ and therefore our photometric value of $z = 2.6$ is a better match than the low value of $z = 0.8$, which would require a V value of 0.05. We also used the absolute magnitude dependence in Figure 11 of Vanden Berk et al. (2004). We estimate an absolute magnitude for our source quasar using the demagnified average of the

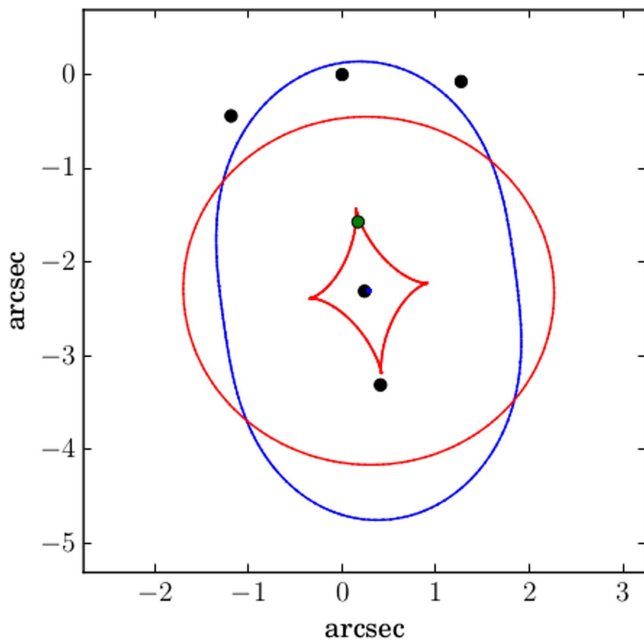


Figure 6. Gravitational lens modeling. The blue and red lines show the critical curves and caustics, respectively. The green dot shows the quasar position in the source plane, and the black dots show the lens and the observed image positions.

observed magnitudes of A, B, and C (see Section 5). Assuming a composite quasar spectrum, we estimate that the *i*-band rest-frame absolute magnitude ranges between -24.8 and -25.2 at redshift 0.8, and between -27.6 and -27.9 at redshift 2.6. Again, we see that the *V* value better matches a high luminosity quasar, and therefore the higher redshift is preferred. We note that in this study we have ignored the variability caused by microlensing (see the next section).

5. Lens Modeling

The results of the previous sections show that the source is likely a quadruply imaged quasar, lensed by a foreground early-type galaxy. We subsequently modeled the observed configuration (the relative positions of the objects A, B, C, D, and G) using the lensmodel software from the gravlens package (Keeton 2001). We chose not to use the observed relative fluxes as constraints, as it is well known that at these wavelengths they usually show large discrepancies due to microlensing, millilensing, intrinsic variability, or extinction (e.g., Sluse et al. 2008). For the mass profile of the lensing galaxy, we use a Singular Isothermal Ellipsoid (SIE) with external shear. There are eight constraints from the four image positions and two constraints from the galaxy position, for a total of 10. Also, there are nine free parameters: two for the galaxy position, one for the Einstein radius, two for ellipticity, two for shear, and two for the source position. The model therefore has one degree of freedom.

For the best-fit mass model parameters, we find an Einstein radius $b = 1.932^{+0.008}_{-0.011}$, ellipticity $e_c = 0.163^{+0.063}_{-0.070}$, $e_s = -0.035^{+0.023}_{-0.024}$, and shear $\gamma_c = 0.122^{+0.015}_{-0.016}$, $\gamma_s = 0.065 \pm 0.005$. Here, we expressed the ellipticity and shear in quasi-Cartesian coordinates, rather than polar coordinates, as the distribution of uncertainties is more Gaussian. The two coordinate systems are related by $(e_c, \gamma_c) = (e, \gamma) \cos 2(\theta_e, \theta_\gamma)$ and $(e_s, \gamma_s) = (e, \gamma) \sin 2(\theta_e, \theta_\gamma)$. The derived image magnifications are

approximately 19, 11, 11, and 0.7 for A, B, C, and D, respectively. The uncertainties were determined using MCMC as plotted in Figure 5, where the convergence of the chains was again checked using the method of Gelman et al. (1995). The χ^2 for this model is 0.8.

While the parameters derived above are independent of redshift, estimating the expected time delays between the images does require redshift information. Using the results of Section 3, we have fixed the redshift of the source at 0.57. If we assume a source redshift of 0.82, according to the best-fit result of the Wu & Jia (2010) method in Section 3, we derive from the expression of the Einstein radius in a singular isothermal profile, $b = 4\pi \left(\frac{\sigma}{c}\right)^2 \frac{D_{ls}}{D_s}$, a velocity dispersion of $\sigma \sim 500 \text{ km s}^{-1}$. Here, c is the speed of light, and D_s and D_{ls} are the angular diameter distances to the source and between the lens and source, respectively. This value is too large for a single galaxy, but if we employ the second-best source redshift estimate, $z \sim 2.6$, which is preferred by LePhare, the combination of *WISE* and *PS1* colors (Section 3), and the variability results in Section 4, we obtain $\sigma \sim 315 \text{ km s}^{-1}$, a more common value for massive early-type galaxies. We therefore assume this redshift to infer the predicted time delays, and we obtain $\Delta t_{BC} = 0.1$ days, $\Delta t_{AC} = 1.7$ days, and $\Delta t_{DC} = 226.2$ days, with image C (a minimum of the time delay surface) leading. Image B is another minimum, and images A and D are saddle points.

In Figure 6, we show the critical curve and the caustics, as well as the positions of the source and the observed images. The source is crossing a cusp, which results in the production of three bright images in close proximity and one isolated faint image. This is a classic configuration for quad lenses. The predicted magnitude differences are shown in Table 1, and a comparison with the observed values are shown in Figure 7.

We find that the predicted brightness ranking of the images is consistent with the observations, with image A being brightest and image D being faintest. However, there are still large discrepancies between the observed and predicted fluxes. For example, the fluxes of images B and C are different, whereas they are expected to be the same for any smooth mass profile of the lensing galaxy. Such “flux anomalies” have been widely encountered for cusp lensed quasars and can be explained by small-scale structure in the lensing galaxy (e.g., Keeton et al. 2003). We also remark that the colors of the four images are very similar, within $\lesssim 0.2$ mag across all filters. Small chromatic variations between multiple quasar images are known to be caused by intrinsic variability, microlensing, or differential extinction (Yonehara et al. 2008). In any case, differential extinction would not explain the flux discrepancy in image D, as this is ~ 1 mag *brighter* than expected. Since image D is closest to the lensing galaxy, the stellar density is comparatively high at its location, meaning that microlensing due to stars in the lensing galaxy is a plausible explanation for the discrepancy. Second, we remark that the time delays between image D and the other images is large, which means that while intrinsic flux variations between A, B, and C will be washed out, they could stand out in image D, and therefore be responsible for the discrepancy. Lastly, small-scale substructure (millilensing) could contribute to the discrepancy.

6. Conclusions and Future Work

We have presented the first quadruply imaged gravitationally lensed quasar candidate in the Pan-STARRS1 Survey, discovered via visual inspection of the multiband images. We

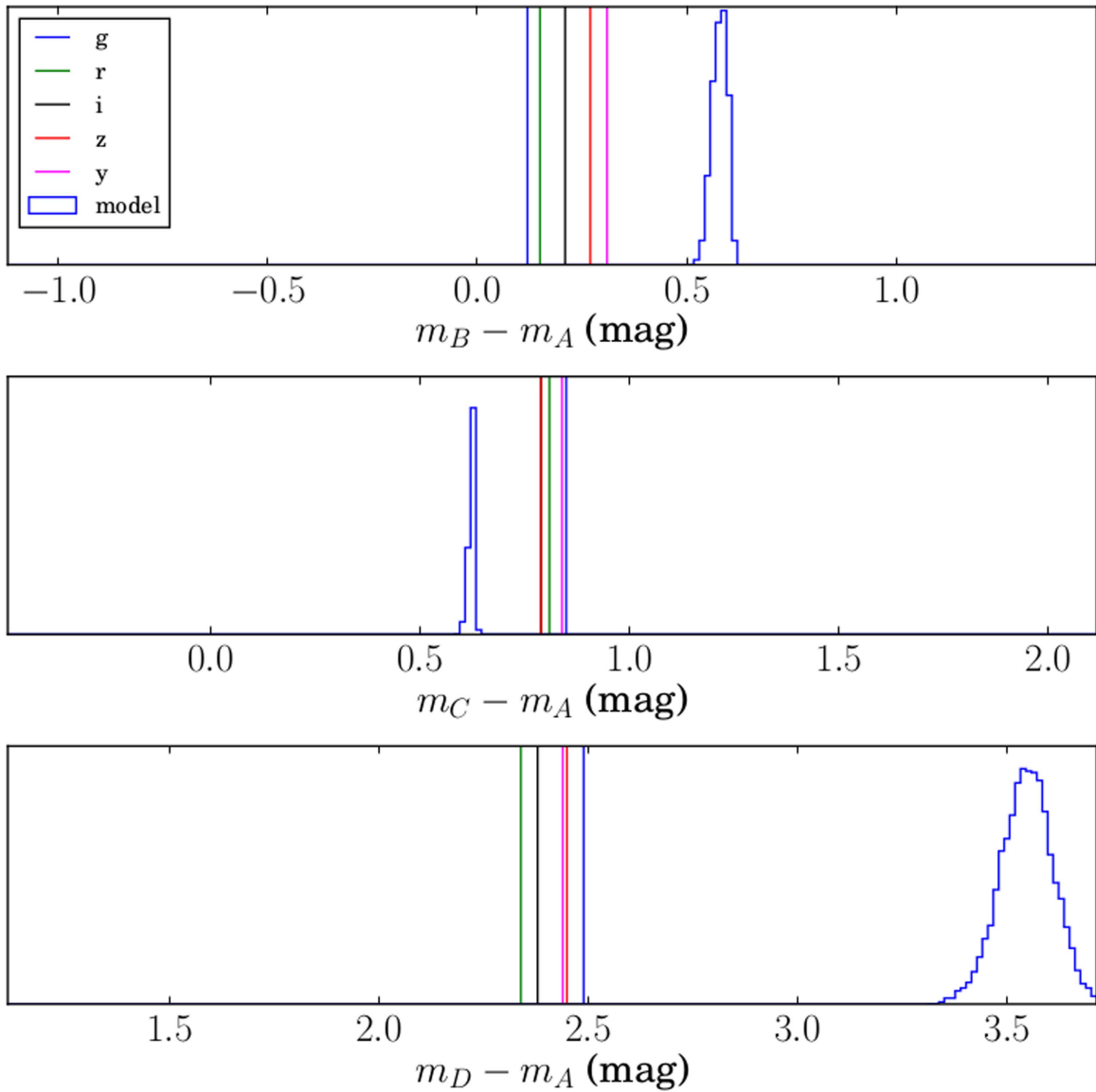


Figure 7. Comparison between the observed quasar image magnitudes relative to image A (vertical colored lines) and the model predictions (blue histogram) for each PS1 band. The model predictions were drawn from an MCMC exploration of the range of models.

find that the evidence supporting the gravitational lens nature of this system is overwhelming and consists of the following.

1. The presence of four point-like images within $\lesssim 3''.8$ of each other, with similar colors, more consistent with quasar templates, but less so with stars and galaxies.
2. The detection of a red galaxy between the point source, such that the relative positions of all five objects are fully consistent with a well-known “cusp” configuration. We successfully reproduce this configuration using a SIE + shear model for the lensing galaxy. Furthermore, the brightness ranking of the point-like images is consistent with the one predicted by the model.
3. The photometric redshift analysis shows that the galaxy is of elliptical template, typical for lensing galaxies, and of redshift smaller than the point sources. For the inferred redshifts (assuming a source redshift of ~ 2.6), the velocity dispersion of the lensing galaxy is consistent with those of massive early-type galaxies.

Nevertheless, we stop short of claiming that this is a confirmed lens until we can obtain spectroscopy of this system. Spectroscopy of the four point-like images would unequivocally demonstrate whether they are multiple images of the same background quasar, as well as allow one to infer its redshift and physical properties. We also note that the system is accessible to ground-based high-resolution observations at most adaptive optics-capable facilities in the northern hemisphere, due to its proximity to a $R \sim 12$ mag star $\sim 18''$ away.

In the introduction, we noted its similarity with RX J1131-1231; however, our system appears to have a larger source redshift and images brighter by about 2 mag (Sluse et al. 2006). Sluse et al. (2008) also measure flux discrepancies for RX J1131-1231 and show that these flux discrepancies can be explained by microlensing.

We would like to thank Arunav Kundu, Shobita Satyapal, Nathan Secrest, Bryan Dorland, and Valeri Makarov for useful discussions and help. We also thank the referee for great

suggestions. C.E.R. was funded through the NSF grant AST-1312329, “Collaborative Research: Accurate cosmology with strong gravitational lens time delays,” and the *HST* grant GO-12889.

The Pan-STARRS1 Surveys (PS1) and the PS1 public science archive have been made possible through contributions by the Institute for Astronomy, the University of Hawaii, the Pan-STARRS Project Office, the Max-Planck Society and its participating institutes, the Max Planck Institute for Astronomy, Heidelberg and the Max Planck Institute for Extraterrestrial Physics, Garching, The Johns Hopkins University, Durham University, the University of Edinburgh, the Queen’s University Belfast, the Harvard-Smithsonian Center for Astrophysics, the Las Cumbres Observatory Global Telescope Network Incorporated, the National Central University of Taiwan, the Space Telescope Science Institute, the National Aeronautics and Space Administration under Grant No. NNX08AR22G issued through the Planetary Science Division of the NASA Science Mission Directorate, the National Science Foundation Grant No. AST-1238877, the University of Maryland, Eotvos Lorand University (ELTE), the Los Alamos National Laboratory, and the Gordon and Betty Moore Foundation.

This work has made use of data from the European Space Agency (ESA) mission *Gaia* (<https://www.cosmos.esa.int/gaia>), processed by the *Gaia* Data Processing and Analysis Consortium (DPAC; <https://www.cosmos.esa.int/web/gaia/dpac/consortium>). Funding for the DPAC has been provided by national institutions, in particular the institutions participating in the *Gaia* Multilateral Agreement.

References

- Agnello, A., Treu, T., Ostrovski, F., et al. 2015, *MNRAS*, **454**, 1260
- Arnouts, S., Cristiani, S., Moscardini, L., et al. 1999, *MNRAS*, **310**, 540
- Benítez, N. 2000, *ApJ*, **536**, 571
- Bertin, E., & Arnouts, S. 1996, *A&AS*, **117**, 393
- Bonvin, V., Courbin, F., Suyu, S. H., et al. 2017, *MNRAS*, **465**, 4914
- Brewer, B. J., & Lewis, G. F. 2008, *MNRAS*, **390**, 39
- Chambers, K. C., Magnier, E. A., Metcalfe, N., et al. 2016, arXiv:1612.05560
- Chiba, M., Minezaki, T., Kashikawa, N., Kataza, H., & Inoue, K. T. 2005, *ApJ*, **627**, 53
- Claeskens, J.-F., & Surdej, J. 2002, *A&ARv*, **10**, 263
- Condon, J. J., Cotton, W. D., Greisen, E. W., et al. 1998, *AJ*, **115**, 1693
- Dai, X., Kochanek, C. S., Chartas, G., et al. 2010, *ApJ*, **709**, 278
- Ding, X., Treu, T., Suyu, S. H., et al. 2017, *MNRAS*, submitted (arXiv:1703.02041)
- DiPompeo, M. A., Bovy, J., Myers, A. D., & Lang, D. 2015, *MNRAS*, **452**, 3124
- Faber, S. M., & Jackson, R. E. 1976, *ApJ*, **204**, 668
- Fadely, R., & Keeton, C. R. 2012, *MNRAS*, **419**, 936
- Finch, C. T., & Zacharias, N. 2016, AAS meeting, 47, 203.03
- Finkbeiner, D. P., Schlafly, E. F., Schlegel, D. J., et al. 2016, *ApJ*, **822**, 66
- Foreman-Mackey, D. 2016, *JOSS*, **24**
- Gaia Collaboration, Brown, A. G. A., Vallenari, A., et al. 2016, *A&A*, **595**, A2
- Gelman, A., Carlin, J. B., Stern, H. S., et al. 1995, *Bayesian Data Analysis* (Boca Raton, FL: CRC Press)
- Ilbert, O., Arnouts, S., McCracken, H. J., et al. 2006, *A&A*, **457**, 841
- Keeton, C. R. 2001, arXiv:astro-ph/0102340
- Keeton, C. R., Gaudi, B. S., & Petters, A. O. 2003, *ApJ*, **598**, 138
- Kochanek, C. S., Falco, E. E., Impey, C. D., et al. 2000, *ApJ*, **543**, 131
- McKean, J. P., Koopmans, L. V. E., Flack, C. E., et al. 2007, *MNRAS*, **378**, 109
- Moffat, A. F. J. 1969, *A&A*, **3**, 455
- More, A., Oguri, M., Kayo, I., et al. 2016, *MNRAS*, **456**, 1595
- Myers, S. T., Jackson, N. J., Browne, I. W. A., et al. 2003, *MNRAS*, **341**, 1
- Oguri, M. 2010, *PASJ*, **62**, 1017
- Oguri, M., & Marshall, P. J. 2010, *MNRAS*, **405**, 2579
- Oguri, M., Rusu, C. E., & Falco, E. E. 2014, *MNRAS*, **439**, 2494
- Oguri, M., Inada, N., Pindor, B., et al. 2006, *AJ*, **132**, 999
- Oguri, M., Inada, N., Strauss, M. A., et al. 2012, *AJ*, **143**, 120
- Onaka, P., Tonry, J. L., Isani, S., et al. 2008, *Proc. SPIE*, **7014**, 12
- Peng, C. Y., Ho, L. C., Impey, C. D., & Rix, H.-W. 2010, *AJ*, **139**, 2097
- Peng, C. Y., Impey, C. D., Rix, H.-W., et al. 2006, *ApJ*, **649**, 616
- Reis, R. C., Reynolds, M. T., Miller, J. M., & Walton, D. J. 2014, *Natur*, **507**, 207
- Richards, G. T., Myers, A. D., Gray, A. G., et al. 2009, *ApJS*, **180**, 67
- Rusu, C. E., Oguri, M., Minowa, Y., et al. 2016, *MNRAS*, **458**, 2
- Schlafly, E. F., & Finkbeiner, D. P. 2011, *ApJ*, **737**, 103
- Secrest, N. J., Dudik, R. P., Dorland, B. N., et al. 2015, *ApJS*, **221**, 12
- Sérsic, J. L. 1963, *BAAA*, **6**, 41
- Sluse, D., Claeskens, J.-F., Altieri, B., et al. 2006, *A&A*, **449**, 539
- Sluse, D., Eigenbrod, A., Courbin, F., et al. 2008, *Manchester Microlensing Conf. 20, 12th Int. Conf. and ANGLES Microlensing Workshop*, ed. E. Kerins et al. (Trieste: PoS), **20S**
- Sluse, D., Hutsemékers, D., Courbin, F., Meylan, G., & Wambsganss, J. 2012, *A&A*, **544**, A62
- Sluse, D., Surdej, J., Claeskens, J.-F., et al. 2003, *A&A*, **406**, L43
- Sonnenfeld, A., Chan, J. H. H., Shu, Y., et al. 2017, *PASJ*, submitted (arXiv:1704.01585)
- Tonry, J., & Onaka, P. 2009, in *Proc. Advanced Maui Optical and Space Surveillance Technologies Conf.*, ed. S. Ryan (Kihei, HI: The Maui Economic Development Board), **E40**
- Treu, T. 2010, *ARA&A*, **48**, 87
- Treu, T., & Marshall, P. J. 2016, *A&ARv*, **24**, 11
- Vanden Berk, D. E., Wilhite, B. C., Kron, R. G., et al. 2004, *ApJ*, **601**, 692
- Walsh, D., Carswell, R. F., & Weymann, R. J. 1979, *Natur*, **279**, 381
- Wu, X.-B., Hao, G., Jia, Z., Zhang, Y., & Peng, N. 2012, *AJ*, **144**, 49
- Wu, X.-B., & Jia, Z. 2010, *MNRAS*, **406**, 1583
- Yonehara, A., Hirashita, H., & Richter, P. 2008, *A&A*, **478**, 95
- York, D. G., Adelman, J., Anderson, J. E., Jr., et al. 2000, *AJ*, **120**, 1579
- Zacharias, N., Finch, C., Subasavage, J., et al. 2015, *AJ*, **150**, 101